Evaluation of a deep-water wave breaking criterion

Zhigang Tian,[1] Marc Perlin,[1] and Wooyoung Choi[2]
[1]*Naval Architecture and Marine Engineering, University of Michigan, Ann Arbor, Michigan 48109, USA*
[2]*Department of Mathematical Sciences, New Jersey Institute of Technology, Newark, New Jersey 07102, USA*

(Received 19 November 2007; accepted 13 May 2008; published online 25 June 2008)

An experimental and numerical study is presented to investigate the breaking criterion of Song and Banner [J. Phys. Oceanogr. **32**, 2541 (2002)] who suggested a threshold range of $(1.4 \pm 0.1) \times 10^{-3}$ for a predictive wave breaking parameter, measuring the rate of change in the local energy maximum and the local wave number, to differentiate between wave trains that lead to breaking and those that do not. To examine the breaking criterion experimentally, four separate wave groups of progressive surface gravity waves with slowly decreasing frequency are generated mechanically in a two-dimensional wave tank. Surface elevations as a function of time are measured using capacitance wave probes; surface elevations as a function of space prior to and during breaking are obtained by recording subregions with an imaging system and combining the measurements from repeated experiments. In addition, nonlinear numerical solutions for the surface elevation profiles for the four wave groups are obtained by solving a set of nonlinear evolution equations using a pseudospectral method and are compared to experiments and linear predictions. It is found that the breaking criterion of Song and Banner is sensitive to the choice of the local wave number, but that a particular local wave number based on the local wave geometry distinguishes wave groups leading to breaking from wave groups that do not break. It is shown that the lead time between the parameter exceeding the threshold and incipient wave breaking increases as wave breaking intensifies. The total energy loss is related strongly to this parameter immediately prior to breaking. © *2008 American Institute of Physics*. [DOI: 10.1063/1.2939396]

I. INTRODUCTION

Many criteria for predicting the onset of breaking and breaking severity of deep-water surface waves have been reported based on field observations, laboratory experiments, and numerical studies. A literature review of work prior to 1998 can be found in the study by Nepf *et al.*[1] Later, Wu and Nepf[2] segregated these criteria into three classes (i.e., geometric, kinematic, and dynamic criteria) based on relevant wave characteristics, such as local wave geometry, wave steepness, wave crest particle velocity and phase speed, wave crest acceleration, and rate of change in momentum and energy. Their experimental study suggested that the kinematic criterion is the most robust while the other two classes are affected readily by wave directionality.

The aforementioned kinematic criterion is used often to predict wave breaking and simply states that breaking occurs when the horizontal crest particle velocity U exceeds the phase speed C. Application of this criterion to irregular waves is complicated due to ambiguity in defining the phase velocity and difficulty in measuring the crest particle velocity. Particle image velocimetry (PIV) measurements by Perlin and He[3] showed that the horizontal velocity at the tip of an overturning jet of their deep-water plunger was 1.3 times the phase speed, while Chang and Liu[4] provided a horizontal particle velocity 68% greater than the phase velocity. Wu and Nepf[2] experimentally validated the kinematic criterion and for three-dimensional seas reported that wave directionality, as well as wave focusing and diffracting, has little affect on the criterion. However, Stansell and MacFarlane[5] reported $U/C \leqslant 0.95$ for spilling breakers and $U/C \leqslant 0.81$ for plunging breakers, which indicate that the kinematic criterion is in general unable to predict the onset of breaking. In addition, Oh *et al.*[6] recently conducted experiments to examine breaking criteria for deep-water wind waves under strong wind action using a PIV system. They also concluded that the kinematic criterion is an inadequate predictor of breaking for wind waves under strong wind action.

Another group of breaking criteria is that of geometric classification. The geometric criteria generally use wave steepness and local wave geometry as characteristic parameters to predict breaking onset. Criteria based on wave steepness ka with values of 0.443,[7] 0.31,[8] 0.43,[9] and 0.41 (Ref. 10) have been reported to indicate the onset of wave breaking. Commonly, the disparity in the breaking ka value is attributed to the various mechanisms responsible for wave breaking and the manner in which the responsible process is generated. In addition, instability,[11] three-dimensional effects,[1] and wave directionality[2,12] are known to have significant influence on the breaking onset. Another factor that strongly affects breaking is the presence of currents, as can be seen at inlet entrances during ebb tide. In particular, Yao and Wu[13] investigated the effects of shear current on the incipient breaking of unsteady waves and found that the steepness at incipient breaking is decreased by a positive shear and increased by a negative shear.

Rapp and Melville[14] showed that global spectrum-based

wave steepness ka_c is a good indicator of breaking onset as well as breaking severity for two-dimensional (2D) unsteady breakers. Chaplin[15] and Kway *et al.*[16] examined deep-water breaking waves of different wave spectra. Both results illustrated that the steepness is sensitive to wave spectral shape. Nepf *et al.*[1] and Wu and Nepf[2] reported similar observations, and they also demonstrated that wave directionality has an effect on the breaking steepness criterion.

Several researchers have demonstrated also that profile asymmetry is important in breaking. Wave steepness defined simply as ka cannot represent the horizontal and the vertical wave crest asymmetries that appear as waves approach incipient breaking. Kjeldsen and Myrhaug[17] introduced the crest front steepness, the crest rear steepness, the vertical asymmetry, and the horizontal asymmetry to describe the asymmetries. However, their parameters were reported to vary considerably and are also sensitive to wave directionality and shape of the wave spectrum.[2,12] Additionally, Yao and Wu[13] showed that sheared currents have pronounced effects on the wave crest asymmetry, and hence on breaking.

Criteria based on energy and energy gradients have created more and more excitement. Schultz *et al.*[18] proposed that the local mean rms potential energy can function as a breaking criterion for regular 2D deep water waves based on numerical experiments of fully nonlinear irrotational flow in a periodic domain. They found that the energy input rate can indicate the breaking severity and suggested a breaking criterion of the potential energy exceeding 52% of the total energy of a limiting Stokes wave.

Focusing also on energy, Banner and Tian[19] investigated the evolution of the local mean energy and momentum densities of modulating surface gravity water waves with the numerical code of Dold.[20] They developed two dimensionless growth rates, β_E and β_M, that are diagnostic parameters of their wave breaking criterion. A threshold of $\beta_{(E/M)}$ equal to 0.2 is reported as a universal criterion, independent of wave group structures, initial wave group configurations, and surface shears. The criterion can also provide information on when wave breaking will occur, as it monitors the evolution of the predictive parameters.

Following similar reasoning, Song and Banner[21] extended the investigation of Banner and Tian by considering a dimensionless growth rate $\delta(t)$ constructed from the evolution of the local energy density and the local wave number at the envelope maxima of three types of deep-water wave groups. A threshold range for $\delta(t)$ of $(1.4 \pm 0.1) \times 10^{-3}$ was suggested to differentiate wave breaking from nonbreaking. Numerical experiments showed that the initial wave group structures, as well as the number of waves in the wave groups, wind forcing, and surface shear,[22] have no effect on the threshold, which suggests that the criterion is universal. For the first time, they systematically reported the lead time between $\delta(t)$ exceeding the threshold value and the onset of wave breaking. In addition, a strong correlation was presented between the breaking parameter $\delta(t)$ and the breaking intensity observed by Rapp and Melville.[14]

During the course of this study, it was discovered that Banner and Peirson[23] conducted detailed laboratory experiments aimed at validating the breaking criterion proposed by Song and Banner. Their intent was to generate and examine two types of wave group structures with the same (equivalent) initial conditions as in Song and Banner's numerical simulations. The total local energy density and the local wave number were inferred based on measurements from six wave probes, designed in a special configuration of two inline sets of three probes. Experimental results were found to be in good agreement with the numerical results of Song and Banner, despite small differences in the conditions.

In this study, there is no intent to examine the evolution of the breaking parameter of the wave groups with the same initial conditions. Rather, the study is designed to validate or not the breaking criterion through experiments on wave groups of differing configuration. Additionally numerical solutions of the Euler equations are obtained using a pseudospectral method by initializing the numerical model with laboratory measurements and are compared carefully to experiments to test the validity of the numerical results near the onset of wave breaking. The remainder of the paper is as follows. Section II describes the experimental strategy, the breaking wave generation method, the physical setup, and the measurement error analysis. Numerical simulations and computation of breaking parameters are presented in Secs. III and IV, respectively. Results and discussion are provided in Sec. V. Section VI communicates our concluding remarks.

II. EXPERIMENTS

Experiments are conducted in a 2D wave tank of length of 35 m, width of 0.7 m, and water depth of 0.62 m. The walls and bottom of the tank are glass; thus, surface elevation profiles can be viewed and recorded unimpeded using imaging systems positioned outside the tank. A servocontrolled wavemaker (oscillating wedge) with a feedback loop and auxiliary electronics is used to generate the wave trains.

The technique to generate breaking waves used by Perlin and He[3] is employed in the experiments. First, a time history of the water surface elevation required at the wavemaker to produce a steep wave at a desired position in the tank is generated. Second, a wavemaker transfer function is applied to obtain the command signal. The local wave steepness ka is further modified such that it approximately remains constant for every zero-upcrossing wave in the wave group. As demonstrated by Perlin and He,[3] the technique helps ensure that the phase speed of each component in the wave group, as well as the local wave steepness ka, will vary equally when the gain of the command signal is altered. One advantage of this method is that it can generate "clean" breaking waves. Here, clean indicates the absence of upstream breaking. This technique is also able to produce breaking waves with strong spatial and temporal repeatability, which is important in this study.

The range of frequencies that comprises the wave group is 1.0–2.0 Hz; therefore, deep-water conditions are maintained as predicted by linear theory for the set water depth. (However, a finite-depth effect was observed when predicting the surface elevations and is addressed subsequently.) A typical command signal to the wavemaker is shown in Fig. 1. Gains (i.e., relative voltages) of 900, 1265, 1650, and 2020

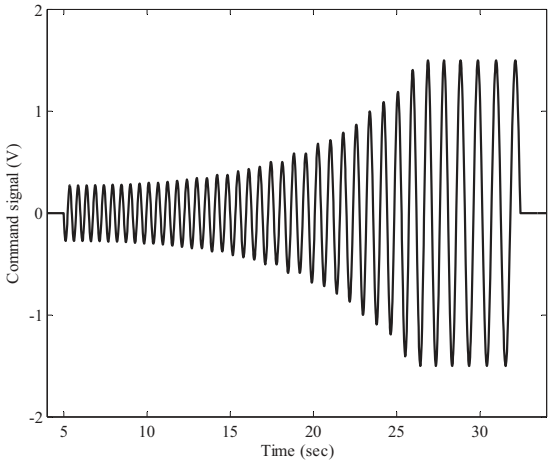

FIG. 1. Typical command signal sent to the wavemaker.

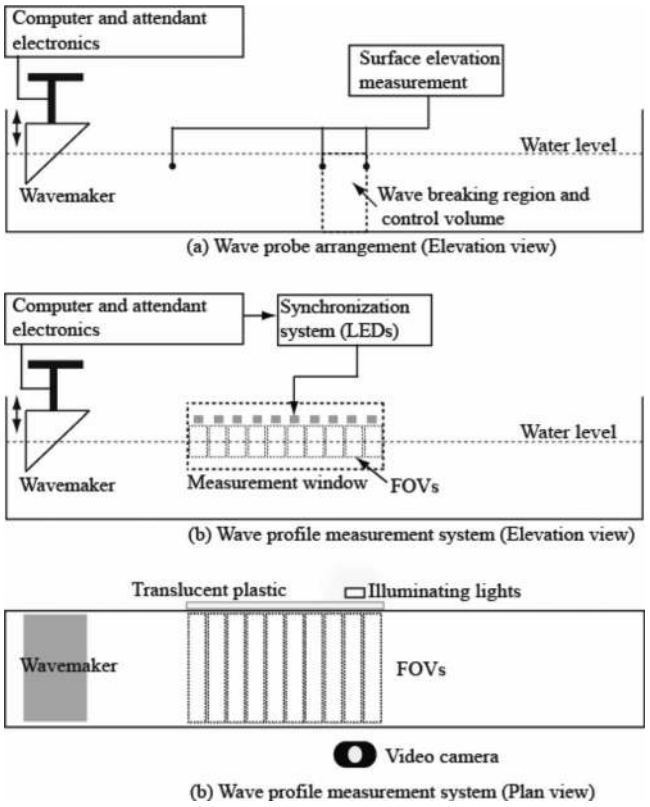

FIG. 2. Sketch of the experimental setup for the (a) temporal and (b) spatial imaging of the sea-surface elevation. FOV indicates the field of view.

are used, corresponding to waves of nonbreaking, breaking, strong breaking, and severe breaking, respectively. The three breakers are plungers and break essentially once, though a following gentle spiller was observed in the gain of 2020 case.

The study is designed to use measured surface elevations (temporal and spatial) to construct the surface profile as a function of time and space, and then to examine the evolution of the parameters that determine the wave breaking onset. In particular, spatial measurements of the surface elevation required to test Song and Banner's breaking criterion[21] are made using video imaging (see Sec. II B).

A. Temporal surface elevation measurements

To measure temporal surface elevations, capacitance wave probes are positioned at desired measurement locations along the tank. The first probe is 6.88 m downstream from the mean wavemaker position (unless specified otherwise, distance x is relative to the mean wavemaker position, and time t refers to the start of the wavemaker). The positions of the second and third gauges are chosen so that the former is upstream and the latter is downstream relative to the wave breaking location. The distance between these two probes is 1.1 m. We note that the positions of the second and third gauges are not fixed as the breaking location of the wave trains with different gains varies. (The change in breaking locations was observed also by others.[14,16]) A sketch of the arrangement is shown in Fig. 2(a). A Dell PC, a National Instruments PCI-6034 board, and an SCB-68 box (NIDAQ-instruments) serve as the data acquisition system to record the temporal measurements.

The recorded temporal surface elevations at the first wave probe are shown in Fig. 3. Based on linear wave theory (LWT), after it is Fourier decomposed into N (256) sinusoidal components, the measured surface elevation can be used to predict the surface elevation as a function of time and space by means of

$$\eta(t,x) = \sum_{n=1}^{N} A_n \cos[\omega_n t - k_n(x - x_m) - \varepsilon_n], \tag{1}$$

where x_m is the position of the wave probe and the nth Fourier component has radian frequency ω_n, wave amplitude A_n, and phase shift ε_n. The temporal surface elevations are measured for a sufficiently long period to ensure that the periodicity in the Fourier analysis does not affect the prediction (i.e., there is only one wave group propagating in the spatial domain). The linear dispersion relation, $\omega_n^2 = k_n g \tanh(k_n h)$, is used to obtain the wave number k_n.

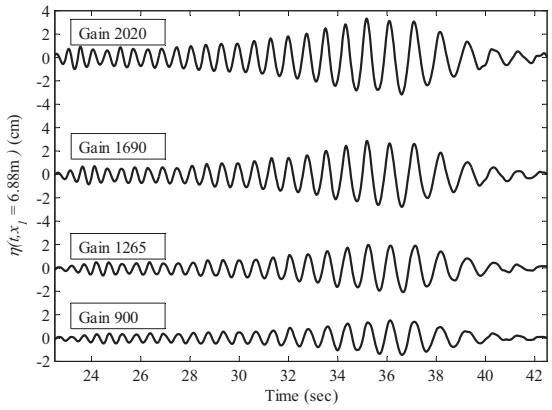

FIG. 3. Measured surface elevations at the first wave probe located at $x_1 = 6.88$ m.

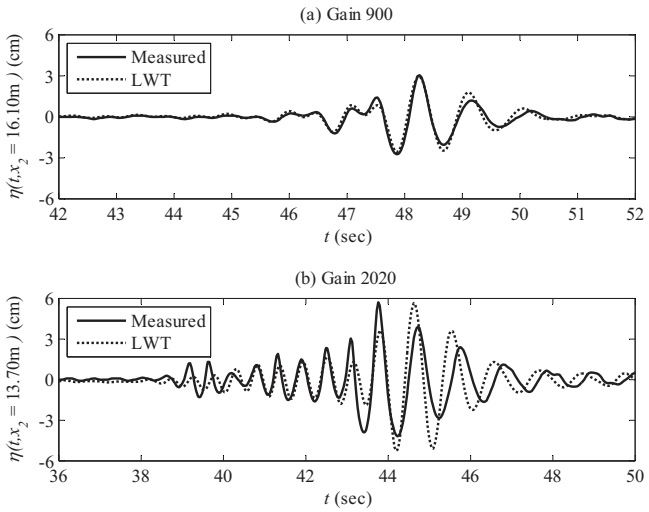

FIG. 4. Measured surface elevations (solid line) compared to the predictions (dashed line) based on LWT at the second wave probe.

To provide comparisons of the measured and predicted surface elevations at the second wave probe, Fig. 4 is presented. In Fig. 4(a), linear theory predicts this profile adequately as the wave steepness is small and nonlinearity effects are negligibly small. As expected, nonlinearity increases with increased wavemaker command signal, and predictions based on LWT become less accurate as the command signal is increased and waves approach breaking. Figure 4(b) illustrates the measured and predicted surface elevations for the severe breaking case. Discrepancies are found in both surface elevation and phase, and therefore, nonlinear theory needs to be introduced.

One problem that attracted our attention was the finite-depth effect in both LWT predictions and numerical simulations. Surface elevations generated according to deep-water conditions deviated from the experimental measurements. Although the carrier wave (frequency of 1.5 Hz) has a wavelength of 0.694 m, which satisfies the deep-water condition ($kh > \pi$) based on LWT, the wave groups exhibit much longer length scales; hence the groups apparently "feel" the tank bottom. Therefore, the linear predictions/simulations are computed using finite-water-depth equations.

For the low command-signal cases, linear theory does an adequate job of describing the surface elevation; thus, the evolution of the breaking parameter may be examined with the predicted surface elevation profiles. However, the parameter $\delta(t)$ for waves of large steepness (the strong and severe breaking cases) can only be determined from accurate spatial measurements, as will be discussed subsequently. That is, to rectify the discrepancies in surface elevation and phase shown to exist using only the temporal probe measurements, spatial measurements are essential.

B. Spatial surface profile measurements

As discussed, for an accurate description of the evolution of the breaking parameter $\delta(t)$, in particular, for large steepness waves, measurements of spatial surface profiles are conducted using the experimental setup depicted in Fig. 2(b). To obtain the surface elevation profiles for this purpose, only those in the final stages of the approach to breaking are recorded, which are related to the total energy dissipation by wave breaking according to Song and Banner.[21] We use spatial information of the surface elevation profiles from approximately the last $7.5T$ (T is the period of the carrier wave with frequency of 1.5 Hz) prior to wave breaking.

The measurement window must be of sufficient length to include as a minimum the entire wave group, approximately $8.5L$ (L is the wavelength of the carrier wave with frequency of 1.5 Hz) in the experiments. It is not possible for us to use a single field of view to achieve this; therefore, the measurement window is divided into ten subregions, each of length of 61 cm. Relying on the demonstrated repeatability of the generated breaking wave process and the measurements in each subregion from repeated runs, we combined the data to construct the surface elevation profile across the entire measurement window.

To facilitate the spatial measurements, a backlighting illumination technique is adopted. This is achieved using a pair of 500 W halogen lights, a sheet of translucent high-density polyethylene, and a video imager. The lights are seated 61 cm from the opposite sidewall with the translucent plastic sheet attached directly to the outer sidewall to diffuse the light and thus backlight the liquid-gas interface. The imager is positioned on the front sidewall of the tank with its axis oriented slightly downward for a better image of the field of view. The imager is framing a field of view of 704 $\times$ 480 pixels at 30 frames/s. Using a precise optical target, the spatial resolution is determined to be 0.866 mm/pixel and the image distortion is shown to be negligible.

This simple method works well for our purposes. The water surface is defined clearly and can be identified easily in the recorded images. When the surface waves become very steep, there is some uncertainty in the wave crest region. However, the uncertainty is limited to ± 3 pixels. Considering that the wave height in the final stage is about 120 mm, this measurement precision (better than 5%) is sufficient for the purposes of this study. [In fact, this method can be used to determine the surface elevation through the breaking process to provide the local potential energy (LPE) density, as we will present in a subsequent publication.]

A synchronization system made of light emitting diodes (LEDs) is utilized to identify simultaneously recorded images. An illumination signal is sent to the LEDs when the wavemaker is initiated, facilitating the synchronization. Since the temporal error from the LEDs is on the order of a microsecond, the measurement error due to time alignment is caused primarily by the framing rate (30 frames/s). To minimize this error, time alignment is carried out carefully by comparing the water surface in the measurement overlap regions. Assuming that the image from the first subregion is measured at time t_0 and measurement of the second subregion starts at time t_1, then the worst scenario is that $\Delta t = t_1 - t_0 = 1/60$ s. A simple analysis for a sinusoidal wave of frequency of 1.5 Hz (i.e., the carrier wave frequency) and wave height of 100 mm (on the order of the maximum wave height in the breaking wave trains) reveals that the error is 7.8% at zero crossings and is 0.1% at maxima, as shown in Fig. 5.

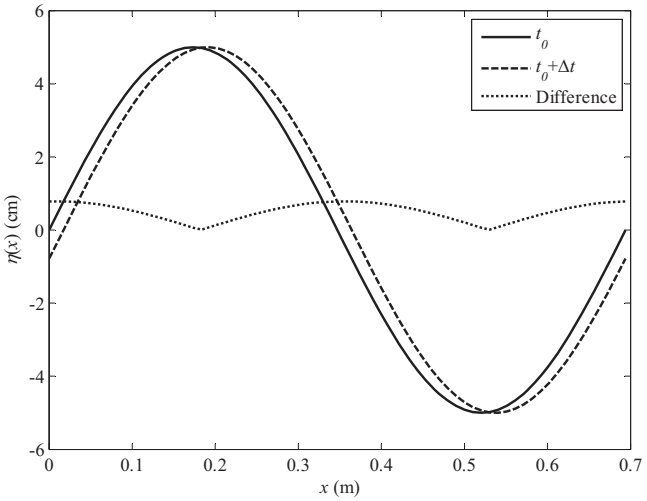

FIG. 5. Illustration of the spatial surface elevation measurement error due to a time alignment inaccuracy for a sine wave. $\Delta t=1/60$ s. Note that the differences of the elevation around the maxima are small.

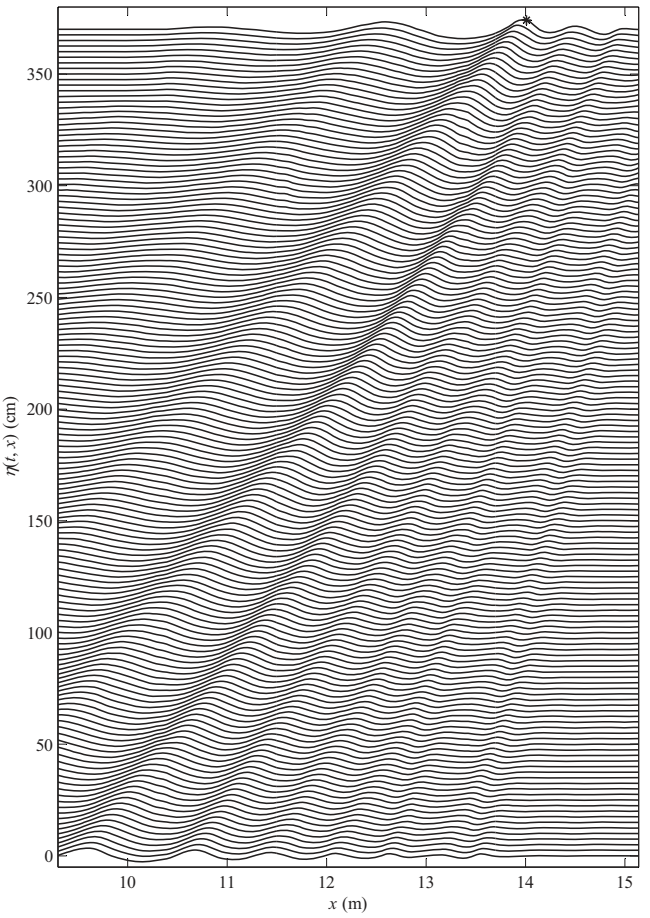

FIG. 6. Measured surface elevations (gain of 2020) as a function of space and time. The asterisk on the uppermost profile shows where incipient breaking occurs. For clarity the surface profiles are offset 2.5 cm for each successive measurement. The time delay between profiles is 1/30 s.

Therefore, the experimental technique presented can capture the wave profile with reasonable precision, especially the wave maxima, which are more important in the calculation of the breaking-prediction parameters.

A series of surface elevation profiles measured with this technique is presented in Fig. 6. The initial profile is measured $7.5T$ before wave breaking ensues, and the time delay between each profile presented is 1/30 s. The asterisk denotes where wave breaking occurs. This waterfall graph presents a clear picture of the temporal evolution of the spatial elevation changes that occur.

III. NUMERICAL SIMULATIONS

Under the ideal-fluid assumption, using a systematic asymptotic expansion in small wave steepness, it was shown[24,25] that the Euler equations with the nonlinear free surface boundary conditions can be reduced to the following nonlinear evolution equations for the surface elevation, $\eta(t,x)$, and the velocity potential evaluated at the free surface, $\Phi(t,x)$:

$$\frac{\partial \eta}{\partial t}=\sum_{n=1}^{\infty} Q_n[\eta,\Phi], \quad \frac{\partial \Phi}{\partial t}=\sum_{n=1}^{\infty} R_n[\eta,\Phi], \tag{2}$$

where Q_n and R_n of $O(ka)^n$ represent the nth order nonlinear terms that can be found through explicit recursion formulas.[26] This system can be considered as an unsteady generalization of the classical Stokes expansion for traveling waves.

After the right-hand sides are truncated to the third order, the system is solved numerically using a pseudospectral method based on the fast Fourier transform to evaluate the right-hand sides and a fourth-order Runge–Kutta method to integrate in time. Since only one wave group is present in the computational domain, the periodic boundary conditions have little effect on the numerical solutions. Higher-order nonlinear computational results show little difference from the third-order solutions even for the strong and severe breaking cases and will not be presented. For details of our numerical method, see Choi *et al.*[26]

To compare the surface elevation profiles with experimental measurements, initial conditions for η and Φ are generated at $t=36$ s using Eq. (1). The computations are performed for a spatial domain of 24 m. Convergence tests illustrate that using 2^{10} points to discretize the domain (i.e., $dx=0.0234$ m) with a time step of 1/60 s is sufficient for the simulation.

A comparison of the computed and measured surface elevation profiles is completed, and the results are presented in Fig. 7 along with the surface elevation profiles predicted by linear theory, as discussed in Sec. II A. For each of the four simulations, as the wave groups approach breaking/near breaking, linear wave predictions become less accurate in terms of both wave heights and phases as a result of the increasing nonlinearity; the agreement between the numerical results and the measurements remains adequate until immediately prior to wave breaking, when the wave crest motion becomes most energetic. For the four wave groups, the disparity between the LWT predictions and the measurements become more pronounced as gain value is increased; contrastingly, numerical simulations consistently provide re-

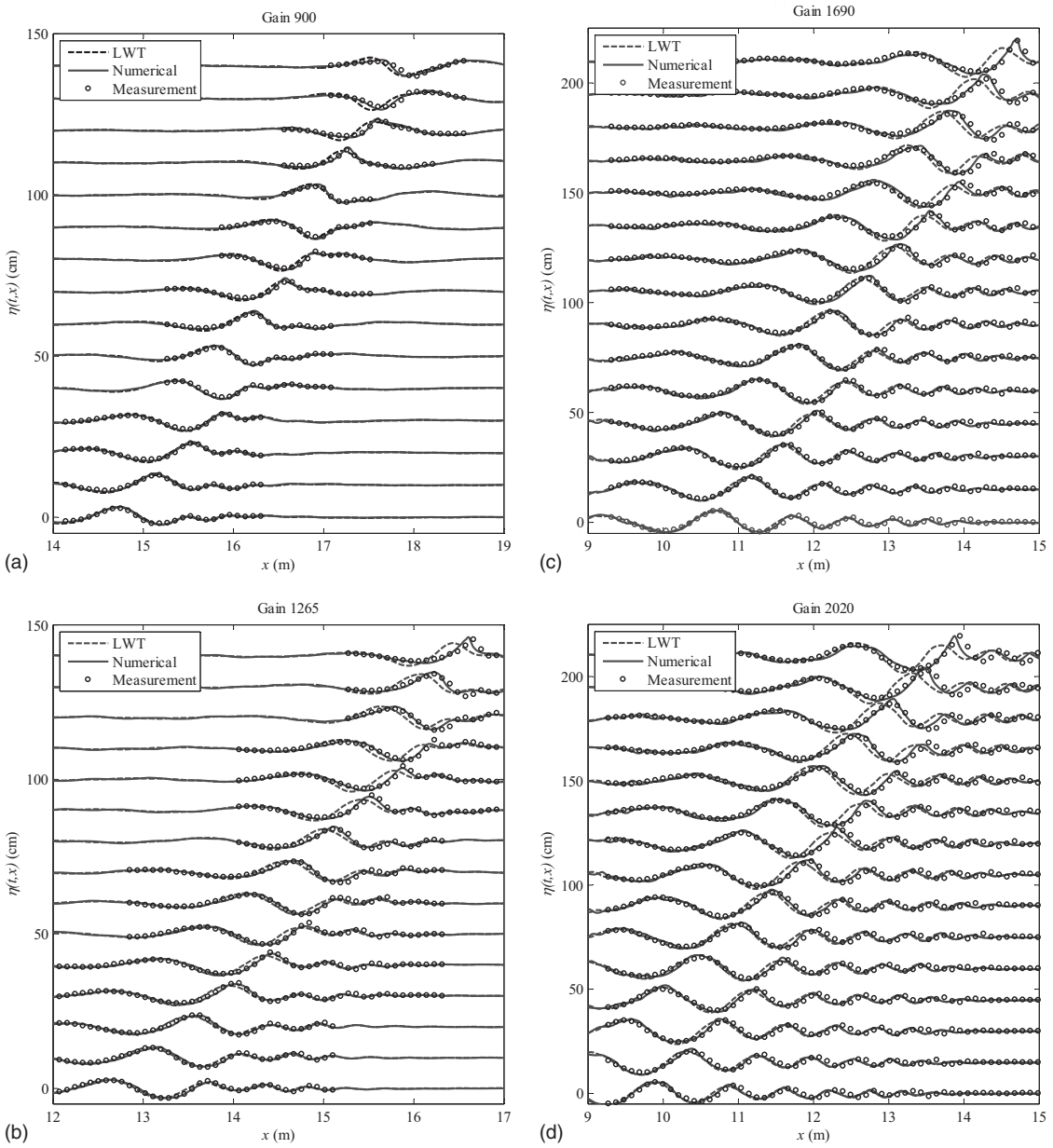

FIG. 7. A comparison of the linear predictions, numerical solutions, and measured surface profiles for the four wave groups. For clarity, one of every six experimental data points is plotted. (a) Gain of 900 results for every $0.5T$ between $70T$ and $77T$ are shown (T is the period of the carrier wave); (b) gain of 1265 results for every $0.5T$ between $65.8T$ and $72.8T$ are shown; (c) gain of 1690 results for every $0.5T$ between $61T$ and $68T$ are shown; (d) gain of 2020 results for every $0.5T$ between $58.7T$ and $65.7T$ are shown. Each profile is offset 15 cm for clarity.

sults closer to the measured values even though the truncated system is obtained under the assumption of small wave steepness.

IV. COMPUTATION OF ASSOCIATED BREAKING PARAMETERS

A. Song and Banner's criterion revisited

Song and Banner[21] proposed a predictive dimensionless parameter $\delta(t)$, which can forecast the onset of wave breaking. A threshold, $\delta_c = (1.4 \pm 0.1) \times 10^{-3}$, is suggested to distinguish a group of waves that will eventually break from a group that will not break, and the threshold is claimed to be independent of the wave group structure. Additionally the parameter is suggested as an indicator of the subsequent breaking intensity that will occur.

In their criterion, the 2D depth-integrated local wave energy density is first found by summing the kinetic and potential energy components of the fluid particles along a vertical line at position x and time t,

$$E(t,x) = \int_{-h}^{\eta} \frac{1}{2}\rho_w (u^2 + w^2) dz + \frac{1}{2}\rho_w g \eta^2, \tag{3}$$

where u and w are the x and z water particle velocity components, g is the gravitational acceleration, ρ_w is the density

of the water, h is the still water depth, and $\eta(t,x)$ is the free surface elevation.

Continuing with their analysis, the parameter s is defined as $s^2=[E/(\rho_w g)]k^2$. As pointed out by Song and Banner, the wave number k is the local wave number, which can be calculated from the x derivative of the unfolded phase function computed from the Hilbert transform of the free surface profile. Another method to obtain the local wave number is to average the physical wave numbers determined from the surface elevation profile by direct measurement of successive crests, troughs, and zero crossings. These two different methods to compute the local wave number will be discussed in detail later.

Of interest are the extreme values of s^2, i.e., $\mu(t) \equiv \max(s^2)$, at each time step. It is known that the maximum of s^2 can be determined either from the maximum of the wave envelope, calculated from the Hilbert transform of the free surface, or from the maximum surface displacement [in this case, $\mu(t)$ is defined as $\mu(t) \equiv (E_{\max}/\rho_w g)k^2$]. As the nonlinear waves approach breaking, the wave envelope and the carrier waves become strongly coupled (i.e., both location and magnitude of the wave envelope maxima approximately match those of the maximum surface displacement); therefore, the wave breaking criterion using the wave properties associated with either wave envelope maxima or maximum surface displacement will result in little difference. In fact, Song and Banner demonstrated that the resulting values of the breaking parameter obtained by tracking either wave envelope maxima or maximum surface displacement are virtually identical. In this paper, following Song and Banner, the latter definition is used to calculate $\mu(t)$ and spline interpolation is used to determine the upper and lower envelopes of $\mu(t)$.

Finally, the local mean $\langle\mu(t)\rangle$ is found by averaging the upper and lower envelopes. [For details on how to calculate the local average value of $\mu(t)$ and $\langle\mu(t)\rangle$, please refer to the work of Song and Banner.[21]] Then the parameter $\delta(t)$ is defined as $\delta(t)=(1/\omega_c)[D\langle\mu(t)\rangle/Dt]$, where ω_c is the center radian frequency of the wave group. As pointed out by Song and Banner, $\langle\mu(t)\rangle$ rather than $\mu(t)$ is used as the primary parameter to compute $\delta(t)$ as the oscillating components of $\mu(t)$ (as seen in both Figs. 11 and 12) are the results of the strong asymmetry of the wave crest and trough, which cannot represent explicitly the energy convergence rate.

B. Surface elevation profiles

Surface elevation profiles are needed to examine whether the proposed threshold of the breaking parameter can distinguish wave breaking from nonbreaking. As described in Sec. III, the surface elevation profiles are obtained using LWT with single point wave-probe measurements, numerical simulations with generated initial conditions, and direct spatial measurements.

With the surface elevation profiles, one can easily detect the maximum surface displacement and its location, and the local wave number can be computed readily once a calculation method is chosen. In the recent work by Banner and Peirson,[23] six wave probes arranged in a special configuration were used to measure the surface elevations. Then the local wave number was deduced from the phase difference in these measurements. Through this strategy, they avoided the issue of measuring the surface elevation field although to apply the approach, the crest and trough maxima of the wave group still need to be found as the group evolves. Notice that their measurement method does not provide spatial zero-crossings-based local wave numbers that are necessary to compute the breaking criterion parameter in the current study.

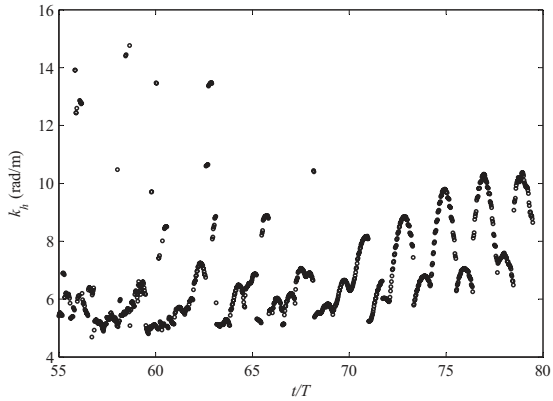

FIG. 8. Local wave number k_h vs dimensionless time. k_h is computed from the numerical solution for gain of 900 using the Hilbert transform at the maximum surface displacement at each time step.

C. Local wave number computation

The breaking parameter $s^2(t)$ is proportional to k^2; therefore accurate computation of local wave number k is extremely important to the wave breaking criterion. In the numerical work by Song and Banner,[21] the local wave number k_h is defined as the derivative of the unfolded phase of the Hilbert transform of the wave group. Although k_h is used in their wave breaking criterion, they applied a low-pass filter to eliminate "spurious" wave numbers with the intention of matching k_h to the local wave number based on the local wave geometry. A similar low-pass filter was applied in the time domain in Banner and Peirson's study,[23] thus limiting the ratio of the local wave number at crest and trough maxima to that of the carrier wave to the range (1, 1.3). Since the choice of filter is somewhat arbitrary, no filter is applied here. The computed k_h at the maximum surface elevation at each time step, for example, for gain of 900, is shown in Fig. 8.

Banner and Tian[19] and Song and Banner[21] also demonstrated that, when filtered properly, the local wave number determined from the Hilbert transform agrees well with that based on successive zero crossings, crests, and troughs. However, the local wave numbers based on the two methods exhibit little agreement for our wave groups, as shown below and in the Appendix.

In this study, the local wave number based on local wave geometry, k_{g1}, is used and it is defined in Fig. 9. The evolution of k_{g1} at the maximum surface displacement for wave

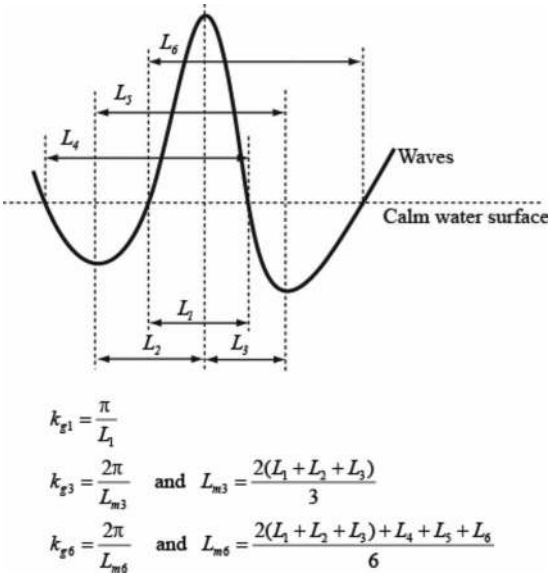

FIG. 9. Definitions of local wave number k_g at the wave crest. The numerical subscripts on k_g represent the number of lengths used in their determination.

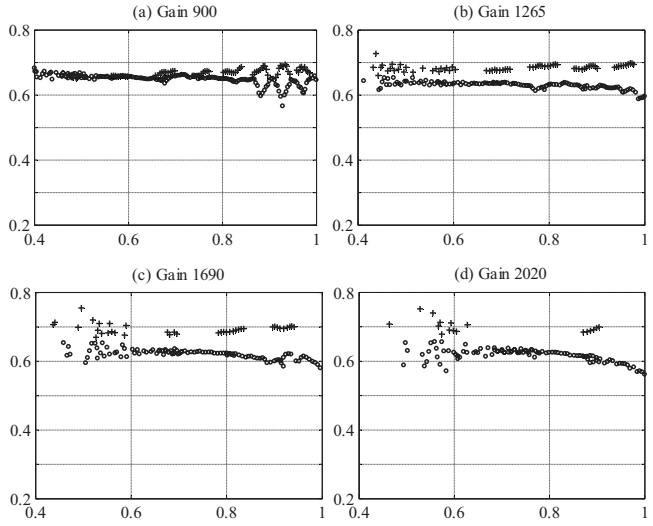

FIG. 11. Ratio of the LPE to the LTE at maximum surface elevations. The abscissa represents the normalized time to wave breaking (or to the focus point if not breaking); the ordinate is the energy ratio. ○ symbols represent the maximum surface elevations at crests; + symbols represent the maximum surface elevations at troughs.

train with gain of 900 is provided in Fig. 10. Note that the intermittent pattern visible in the figure is a result of the maximum surface displacement switching from one wave crest or trough to another during evolution. Other definitions of the local wave number such as k_{g3} and k_{g6} depicted in Fig. 9 are also considered, but, as described in the Appendix, the breaking parameter $\mu(t)$ based on k_{g3} and k_{g6} shows larger time fluctuations. Therefore, k_{g1} is employed to define the local wave number.

As for comparison of k_h and k_{g1}, neither magnitude nor phase is in agreement. The disparity might be due to the application of the Hilbert transform, which only applies to narrow band processes. Wave groups generated in the experiments may not be narrow banded. This problem is known to occur in experiments with breaking wave groups. A discussion on how the breaking parameters vary depending on the choice of local wave number is presented also in the Appendix.

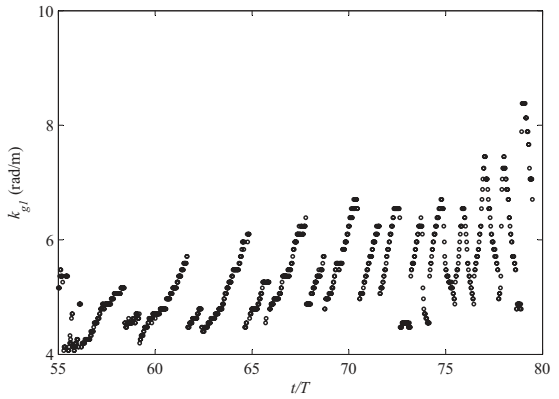

FIG. 10. Local wave number k_{g1} as a function of dimensionless time. k_{g1} is computed from the numerical solution for gain of 900 based on the local wave geometry at the maximum surface displacement. The number of points used for the simulation is 2^{11}. k_g obtained from the simulation results with 2^{10} points is virtually the same.

D. Local energy

This experimental study is intended to examine Song and Banner's breaking wave criterion, where both local potential and local kinetic energy densities are needed. However, simultaneous measurement of both energy densities in such a large domain is very difficult to achieve. In addition, during active breaking, optical techniques to measure particle velocities (e.g., PIV and particle tracking velocimetry) in the immediate vicinity are rendered difficult by the opacity of the (two-phase) flow. Therefore, it is common practice, see experiments on breaking waves by Rapp and Melville,[14] for instance, to obtain total energy by measuring the surface elevations (to determine the potential energy) and by inferring kinetic energy based on wave theory and/or its relationship to potential energy. (A recent work by Banner and Peirson[23] provided experimental validation of their criterion by examining laboratory-generated waves with the same initial conditions as Song and Banner's numerical ones. They also limited their energy measurements to surface elevation measurements.) This method is used for the present study.

In the current investigation, the LPE can be computed easily based on the obtained surface elevations, i.e., $E_p = \rho g \eta^2/2$. To infer the local total energy (LTE) based on the LPE for the experiments, we rely on the numerical simulation results. (Banner and Peirson[23] also used this strategy to determine their LTE.)

Figure 11 presents the numerical results of the ratio of the LPE to the LTE at the maximum surface displacements as the wave group evolves. As wave groups focus, this energy ratio at crest maxima decreases, which means that the local kinetic energy increases. Our results are consistent with those of Banner and Peirson.[23] However, if the maximum

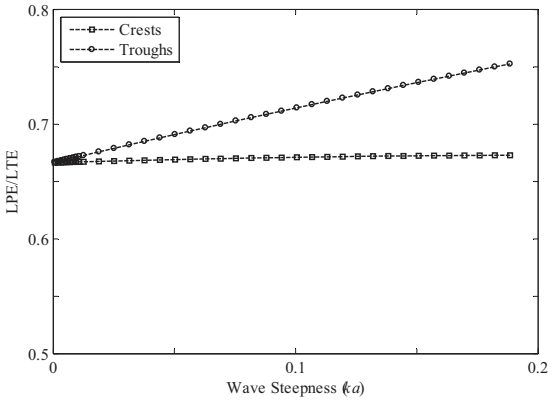

FIG. 12. Ratio of the local LPE to the LTE at crests and troughs for steady third-order Stokes waves. At very small wave steepness ($ka=0.006\,28$), the ratios are approximately equal to 0.667, the same result as given by linear theory.

surface displacement is a wave trough, the ratio of the LPE to LTE as the wave group evolves is quite different than our computations. In the current study, the LPE represents approximately 68% of the total local energy at trough maxima, while Banner and Peirson observed that the ratio at trough maxima decreases from approximately 0.62 to 0.50 as waves evolve to breaking.

As we are somewhat unfamiliar with local analyses as regards water waves, an investigation of a steady third-order Stokes wave was made to provide a comparison of the ratios of the LPE to the LTE at wave crests and troughs. Figure 12 presents those ratios at crests and troughs of waves with different steepness. As shown, the ratio at the crests remains about 66.7% (the ratio from linear theory for deep-water waves is 66.7%) and dwindles slightly as the wave becomes steeper; conversely, the ratio at the troughs varies significantly, from 66.7% to 75.0%, for the cases considered. Based on this observation, one may conclude that the ratio of the LPE to the LTE at crests and troughs can be affected by both wave steepness and the configuration of the wave groups. Having investigated the different ratios for the Stokes solution, we see that the trend is in general agreement with our numerical solution. Therefore, in this paper, the LTE for the experimental study is inferred based on the ratio of the LPE and the total energy found from our numerical results. To do so, we used a third-order polynomial to fit the data (ratio of the LPE to the LTE in Fig. 11) for each wave group, and then the LTE at the wave maxima is computed based on the experimental measurements for the LPE.

V. EXPERIMENTAL EVALUATION OF THE BREAKING CRITERION

A. Examination of the wave steepness as a breaking criterion

To check the breaking criterion based on local wave steepness ka, one can use the measured surface elevation just prior to breaking or at the focus point if there is no breaking. We note that the incipient breaking in this study is defined as when the forward side of the wave crest becomes very steep/vertical but prior to when the crest falls. The wave steepness results are listed in Table I along with $\mu_{\max}^{1/2}$ and $\langle\mu\rangle_{\max}^{1/2}$ the value and the averaged value of the square root of μ immediately prior to wave breaking. Since $\mu(t)$ is defined as $(E_{\max}/\rho_w g)k_{g1}^2$, the square root of $\mu(t)$ and of $\langle\mu\rangle(t)$ are similar to ka, but they are determined from local properties. In the table, a_{backward} and a_{forward} are calculated as one-half of the trough-to-subsequent crest and crest-to-subsequent trough elevations, respectively. Although the wave breaks, the local wave steepness just prior to breaking for the gain of 1265 case is well below the reported criterion threshold.[7,9,10] Although the steepness determined from $k_{g1}a_{\text{backward}}$ for the gain of 1690 group is close to the reported breaking criterion,[7,9,10] the criterion also fails for the maximum dissipation case, gain of 2020 (see Fig. 15). Therefore, we conclude that the wave steepness criterion based on ka does not apply to our wave groups. On the other hand, as one would expect, $\mu_{\max}^{1/2}$ and $\langle\mu\rangle_{\max}^{1/2}$ immediately prior to breaking increase monotonically with increasing gain and seem to be good indicators of nonlinearity.

TABLE I. Local wave steepness immediately before the onset of wave breaking.

Gain	900	1265	1690	2020
$k_{g1}a_{\text{backward}}$	0.2028	0.2893	0.4294	0.4087
$k_{g1}a_{\text{forward}}$	0.1870	0.2243	0.3488	0.3146
$\mu_{\max}^{1/2}$	0.2681	0.3705	0.4680	0.5258
$\langle\mu\rangle_{\max}^{1/2}$	0.2093	0.2781	0.3414	0.4057

B. Examination of Song and Banner's wave breaking criterion

With the surface elevation profiles and local energy, one can examine whether the threshold of the breaking parameter proposed by Song and Banner can distinguish wave breaking from nonbreaking in the four wave groups considered here. Results for the nonbreaking wavetrain, gain of 900, are presented in Fig. 13. The evolution of the breaking parameters, $\mu(t)$ and $\delta(t)$, are computed based on LWT [(a) and (b)] and on numerical simulations [(c) and (d)]; in addition, the parameters obtained from experimental measurements are presented also in (c) and (d). Recall that the breaking parameters are computed with k_{g1} as the local wave number. As shown in Fig. 13, for the nonbreaking experiment, $\delta(t)$ decreases after it achieves its maximum, which is well below the threshold given by Song and Banner. Comparison reveals that linear theory underestimates the energy convergence rate. In addition, an oscillation in $\mu(t)$ caused by wave crest-trough asymmetry[21] is observed; however, the oscillating period based on linear theory is approximately T, while the numerical and experimental results provide an oscillating period of $2T$, which is consistent with Song and Banner.

For the three breaking wavetrains, evolution of the $\langle\mu(t)\rangle$ and $\delta(t)$ is obtained from numerical simulations and direct measurements of the surface profiles, as provided in Fig. 14. For all cases, the $\delta(t)$ parameter achieves its maxi-

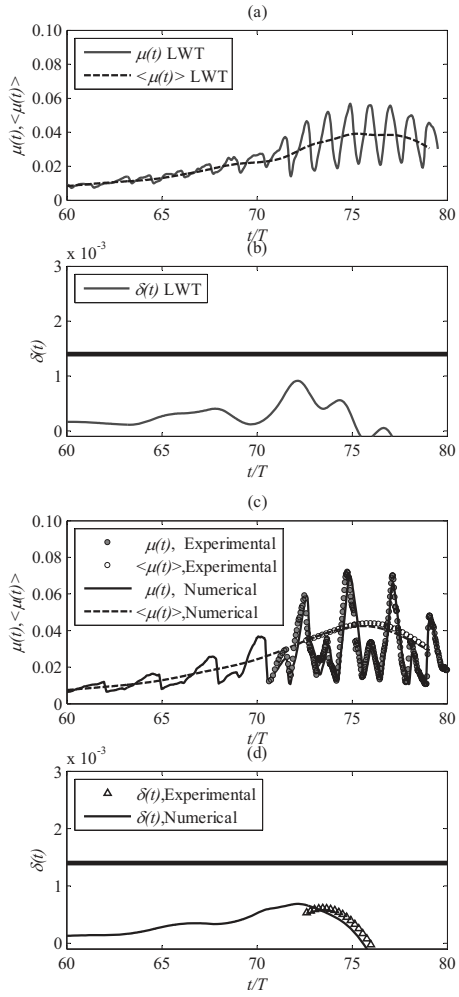

FIG. 13. The growth rate of the breaking parameter $\delta(t)$ for the wave group with gain of 900. Graphs (a) and (b) are the linear results, while (c) and (d) are the numerical ones. In addition, the breaking parameters determined from direct measurements are presented in (c) and (d). Also shown as a function of dimensionless time are the relevant variables used to determine δ. The horizontal region in (b) and (d) denotes the threshold range of $\delta(t)$.

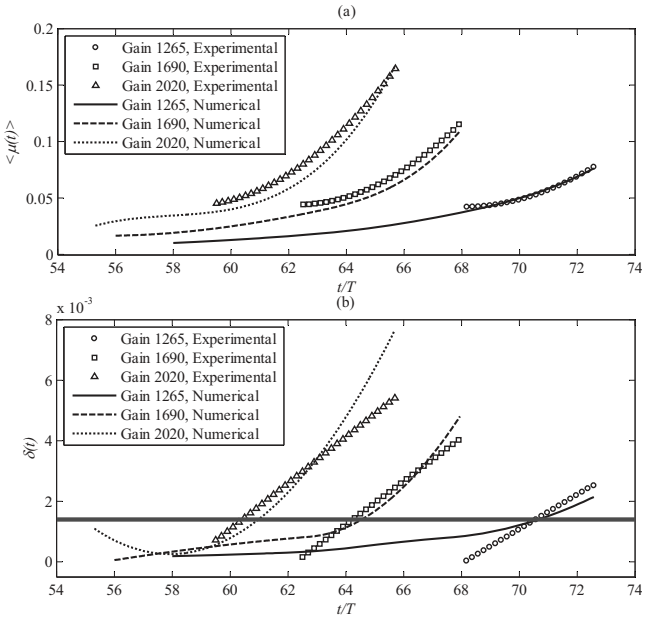

FIG. 14. Evolution of breaking parameters for the breaking wave groups with gains of 1265, 1690, and 2020. The horizontal region in the lower figure denotes the threshold range of $\delta(t)$.

mum at the initiation of wave breaking, and it is greater than the threshold. The numerical results show reasonably good agreement with the measurements before wave breaking occurs. It is noteworthy that the numerical model ran beyond the physical time of breaking (with some energy dissipation due to a low-pass filter that is used primarily to reduce aliasing errors and effectively removes physical energy of high-wave-number components). These experimental results validate that $\delta(t)$ can distinguish breaking wave groups from nonbreaking ones, and verify the prediction by Song and Banner although careful choices of the local wave number and LTE are required.

In Table II, detailed comparisons of the breaking parameters are presented. Here, threshold time is defined as when $\delta(t)$ crosses the threshold value; the breaking time is the actual time (referenced to the start of wave generation) when waves break in the experiments. The lead time between the parameter exceeding the threshold and wave breaking varies significantly for the three breakers. This might indicate that a stronger breaking condition has a longer lead time. However, no similar conclusion is proposed by Song and Banner.[21]

C. Energy dissipation due to wave breaking

Another obvious quantity of interest is the total energy dissipation due to the breaking process. Following Rapp and Melville,[14] the total energy loss due to wave breaking is estimated via surface elevation measurements from the second and third wave probes. To compute the total energy dissipated, one determines the total energy flux in and out the control volume shown in Fig. 2(a). The energy flux is defined as

$$F(t,x) = \int_{-h}^{\eta} \left[\frac{1}{2}\rho_w (u^2 + w^2) + \rho_w g z + P \right] u dz, \tag{4}$$

where P is the water wave pressure. For deep water, under the linear assumption, the flux can be approximated by

$$F(t,x) = \tfrac{1}{2}\rho_w g c_g \eta^2, \tag{5}$$

where c_g is the group velocity. This simplification holds except for the breaking (focus) points, and it has an accuracy to the second order, $O[(ka)^2]$ (Rapp and Melville[14]). If the measurement is initiated from quiescent conditions and continues until the return of quiescent conditions, the total energy dissipation equals the difference of the integrations of energy flux with respect to time,

$$E_{\text{loss}} = \int_{t_0}^{t_1} [F(t,x_2) - F(t,x_3)] dt$$

$$= \frac{1}{2}\rho_w g c \int_{t_0}^{t_1} [\eta(t,x_2)^2 - \eta(t,x_3)^2] dt, \tag{6}$$

where E_{loss} is the total energy loss, t_0 and t_1 are the beginning

TABLE II. Comparison of the breaking parameters.

	Gain	$\delta_{max} \times 10^3$	Threshold time (t/T)	Breaking time (t/T)	Lead time (t/T)
Linear theory	900	0.92			
	1265	1.41			
Numerical simulations	900	0.69			
	1265	2.14	70.70		
	1690	5.39	64.50		
	2020	7.64	61.02		
Experiments	900	0.61			
	1265	2.52	70.63	72.57	1.94
	1690	4.05	64.25	67.95	3.70
	2020	5.41	60.40	65.70	5.30

and ending times, and x_2 and x_3 are the locations of the second and third wave gauges. For 2D waves, in the SI system, E_{loss} has units of J/m.

The wave packet energy obtained by means of integration of energy flux just prior to and after wave breaking has been known to show significant variability;[14,16] therefore, energy loss estimated with Eq. (6) may contain large errors. To minimize the errors, wave-probe measurements are made at 23 stations along the wave tank; results of the integrated energy flux at these stations are presented in Fig. 15. A similar method to that used by Banner and Peirson[23] is applied to determine the energy loss due to wave breaking. As shown in Fig. 15, for the breaking cases, the measurements upstream and downstream of wave breaking are fitted with linear least-square regressions, respectively; then the energy losses are estimated by the difference of the data fitted lines across the break point. Viscous dissipation is represented by the fitted curves of the measurements for the nonbreaking wave train.

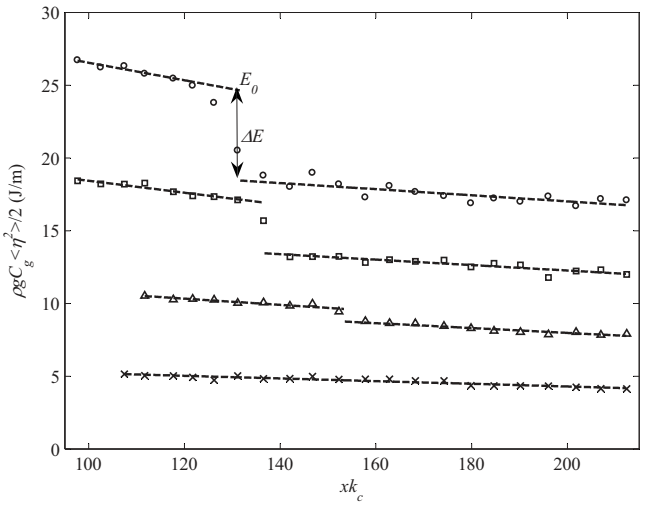

FIG. 15. Estimation of the energy loss due to wave breaking. Wave train measurements with gain of 900 (x); gain of 1265 (△), gain of 1690 [□], and gain of 2020 (○) are shown. Dashed lines represent the linear least-square fits. $\langle \eta^2 \rangle$ is the integration of η^2 with respect to time. E_0 is the integrated energy flux just prior to wave breaking based on the linear least-square fit, and ΔE is the estimated energy loss due to wave breaking, shown only for the gain of 2020 experiment.

Accordingly, the computed total energy loss is nondimensionalized (i.e., $\Delta E/E_0$, where E_0 is the integrated energy flux immediately prior to breaking and ΔE is the estimated energy loss) and compared to the maximum breaking parameter for each of the three breaking cases, as shown in Fig. 16. For these three experiments, the breaking parameter increases as total energy dissipation increases. Similar dependence on the energy loss due to wave breaking of the predictive parameter was also reported by Banner and Peirson.[23] However, for a comparable δ_{max}, our energy loss is almost twice that of Banner and Peirson. The discrepancy may be attributed to generally smaller local wave number (see Figs. 8 and 10 and the impact of the choice of local wave number on the breaking parameter in the Appendix). Another possible cause of the energy dissipation discrepancy is the type of breaking wave that occurs. In the current study, the three breakers are all plungers and break only once; while the wave trains of Banner and Peirson exhibit multiple breaking.

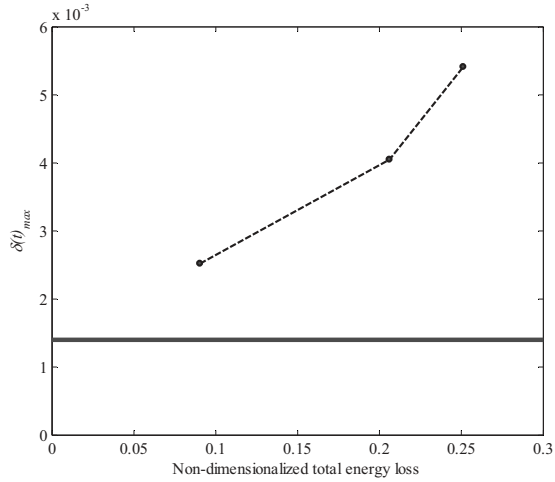

FIG. 16. Nondimensionalized total energy loss vs breaking parameter $\delta(t)_{max}$ (determined from experimental measurements) for the three breaking cases. The horizontal region in the figure denotes the threshold range of $\delta(t)$.

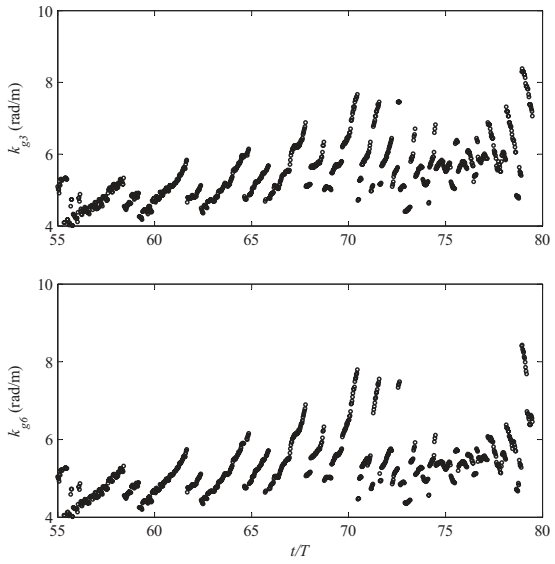

FIG. 17. Same as Fig. 10 but for k_{g3} and k_{g6}. See Fig. 9 for definitions of k_{g3} and k_{g6}.

VI. CONCLUSIONS

An experimental and numerical study of the wave breaking criterion proposed by Song and Banner is presented by examining the growth rate of the breaking parameter $\delta(t)$ constructed from the evolution of the total local energy density and the local wave number at the maximum surface displacement of wave groups. It is found that the breaking criterion of Song and Banner is sensitive to the choice of the local wave number, but that a particular local wave number based on local wave geometry distinguishes wave groups leading to breaking from wave groups that do not break.

The breaking/nonbreaking wave generation technique used in the experiments is capable of producing wave groups with reasonable spatial and temporal repeatability. The repeatability of the generated wave groups enables us to divide the spatial domain into smaller subregions, each of which can be measured individually. Measurements from different runs are combined to obtain the surface elevation spatial profile during the final stages of breaking. Error analysis showed that the measurement technique can provide reasonable precision.

Local wave number computation based on both the Hilbert transform and the local wave profile is discussed; using one of the wave number construction techniques and the local wave profile in conjunction with the parameter of Song and Banner produced reliable wave breaking predictions for our wave groups. Ratios of LPE to LTE at crest maxima and trough maxima are obtained based on numerical simulations. The ratios at crest maxima decrease as the wave groups focus, while there is little variation in the ratios at trough maxima. The local energy at wave maxima for the experimental study is inferred based on numerical simulations.

For the criterion based on local wave geometry, measured surface profiles just prior to incipient breaking are used to determine the local wave steepness. Results show that the wave steepness criterion is unable to differentiate wave breaking from nonbreaking for our wave groups. For Song and Banner's criterion, experimental results illustrate that the energy convergence rate at the maxima increases, and that the corresponding wave geometry steepens. The breaking parameter $\delta(t)$ constructed from the energy convergence rate and the local wave geometry decreases after it achieves a maximum, which is smaller than the threshold for nonbreaking waves; on the other hand, the parameter continues growing once it surpasses the threshold for breaking conditions.

It is shown that the lead time between the parameter exceeding the threshold and incipient wave breaking increases as wave breaking intensifies. A similar relationship exists between the total energy loss and the value of the breaking parameter just prior to wave breaking.

TABLE III. $\delta_{\max}$ determined with k_h and the numerical results.

Gain	900	1265	1690	2020
$\delta_{\max} \times 10^3$	5.20	22.07	21.84	22.18

ACKNOWLEDGMENTS

This investigation was funded by the Office of Naval Research under ONR Contract No. N00014-05-1-0537, a MURI contract awarded to the University of Michigan.

APPENDIX: BREAKING PARAMETERS BASED ON k_{g3} AND k_{g6}

Figure 17 provides the evolution of k_{g3} and k_{g6} (as in Fig. 10 in the text, the evolution is also from the maximum surface displacement). Along with Fig. 10, it is obvious that the three k_g behave similarly to $t/T=70$, after which their evolutions change; the variation in k_{g1} is less than that in k_{g3} and k_{g6}. Careful inspection of the wave profiles reveals that a considerable short wave perturbation occurs just above or below the mean water level after $t/T=70$.

When k_{g6} and k_{g3} rather than k_{g1} are adopted to compute the local wave number, the resulting breaking parameter $\mu(t)$ shows larger time fluctuations, and hence, the resulting breaking criterion parameter does not differentiate breaking waves from nonbreaking ones via Song and Banner's criterion. One possible explanation for this is that not all components of k_{g6} and k_{g3} represent the local character of the geometry, and thus the resulting breaking parameter does not represent the physics.

To test the breaking criterion using the local wave number based on the Hilbert transform, $\delta_{\max}$ is computed with k_h for both the nonbreaking and breaking cases and the numerical results are shown in Table III. Since k_h is in general greater than k_g, $\delta_{\max}$ for the nonbreaking case is much larger than the threshold value of Song and Banner[21] and almost one order of magnitude larger than the one determined with k_{g1} (see Table II) for the same wave group. For the three breaking cases, the determined $\delta_{\max}$ are surprisingly close to each other, which means that the parameter obtained with k_h is not a good indicator of the breaking strength. Noticing the significant difference in $\delta_{\max}$ between the nonbreaking and breaking wave trains, we suspect that a proper threshold for

δ, other than $\delta_c=(1.4\pm0.1)\times10^{-3}$, may be valid for our wave groups if the local wave number is determined with the Hilbert transform without any artificial filtering.

[1] H. M. Nepf, C. H. Wu, and E. S. Chan, "A comparison of two- and three-dimensional wave breaking," J. Phys. Oceanogr. **28**, 1496 (1998).
[2] C. H. Wu and H. M. Nepf, "Breaking criteria and energy losses for three-dimensional wave breaking," J. Geophys. Res. **107**, 3177 (2002).
[3] M. Perlin, J. H. He, and L. P. Bernal, "An experimental study of deep water plunging breakers," Phys. Fluids **8**, 2365 (1996).
[4] K. A. Chang and P. L. F. Liu, "Velocity, acceleration and vorticity under a breaking wave," Phys. Fluids **10**, 327 (1998).
[5] P. Stansell and C. MacFarlane, "Experimental investigation of wave breaking criteria based on wave phase speeds," J. Phys. Oceanogr. **32**, 1269 (2002).
[6] S. H. Oh, N. Mizutani, K. D. Suh, and N. Hashimoto, "Experimental investigation of breaking criteria of deepwater wind waves under strong wind action," Appl. Ocean. Res. **27**, 235 (2005).
[7] G. G. Stokes, "Supplement to a paper on the theory of oscillatory waves," Math. Phys. Papers **1**, 314 (1880).
[8] J. H. Duncan, "An experimental investigation of breaking waves produced by a towed hydrofoil," Proc. R. Soc. London, Ser. A **377**, 331 (1981).
[9] M. Tanaka, "The stability of steep gravity waves," J. Phys. Soc. Jpn. **52**, 3047 (1983).
[10] S. E. Ramberg and O. M. Griffin, "Laboratory study of steep and breaking deep water waves," J. Waterway, Port, Coastal, Ocean Eng. **113**, 493 (1987).
[11] W. K. Melville, "The instability and breaking of deep-water waves," J. Fluid Mech. **115**, 163 (1982).
[12] K. She, C. A. Greated, and W. J. Easson, "Experimental study of three dimensional wave breaking," J. Waterway, Port, Coastal, Ocean Eng. **120**, 20 (1994).
[13] A. Yao and C. H. Wu, "Incipient breaking of unsteady waves on sheared currents," Phys. Fluids **17**, 082104 (2005).
[14] R. J. Rapp and W. K. Melville, "Laboratory measurements of deep water breaking waves," Philos. Trans. R. Soc. London, Ser. A **331**, 735 (1990).
[15] J. Chaplin, "On frequency-focusing unidirectional waves," Int. J. Offshore Polar Eng. **6**, 131 (1996).
[16] J. H. L. Kway, Y. S. Loh, and E. S. Chan, "Laboratory study of deep water breaking waves," Ocean Eng. **25**, 657 (1998).
[17] S. P. Kjeldsen and D. Myrhaug, "Wave-wave and wave-current interactions in deep water," in *Proceedings of the Fifth POAC Conference, Trondheim*, Norway (University of Trondheim, Trondheim, 1979), Vol. III, p. 179.
[18] W. W. Schultz, J. Huh, and O. M. Griffin, "Potential energy in steep and breaking waves," J. Fluid Mech. **278**, 201 (1994).
[19] M. L. Banner and X. Tian, "On the determination of the onset of wave breaking for modulating surface gravity water waves," J. Fluid Mech. **367**, 107 (1998).
[20] J. W. Dold, "An efficient surface-integral algorithm applied to unsteady gravity waves," J. Comput. Phys. **103**, 90 (1992).
[21] J. B. Song and M. L. Banner, "On determining the onset and strength of breaking for deep water waves. Part I. Unforced irrotational wave groups," J. Phys. Oceanogr. **32**, 2541 (2002).
[22] M. L. Banner and J. B. Song, "On determining the onset and strength of breaking for deep water waves. Part II. Influence of wind forcing and surface shear," J. Phys. Oceanogr. **32**, 2559 (2002).
[23] M. L. Banner and W. L. Peirson, "Wave breaking onset and strength for two-dimensional deep water wave groups," J. Fluid Mech. **585**, 93 (2007).
[24] B. J. West, K. A. Brueckner, R. S. Janda, D. M. Milder, and R. L. Milton, "A new numerical method for surface hydrodynamics," J. Geophys. Res. **92**, 11803, DOI: 10.1029/JC092iC11p11803 (1987).
[25] W. Choi, "Nonlinear evolution equations for two-dimensional surface waves in a fluid of finite depth," J. Fluid Mech. **295**, 381 (1995).
[26] W. Choi, C. P. Kent, and C. Schillinger, *Advances in Engineering Mechanics* (World Scientific, Singapore, 2005), p. 94.